

# Multimodal 5-DOF Stretchable Electromagnetic Actuators toward Haptic Information Delivery

*Si Chen, Li Yu, Weijun Shen, Brian Fong, Yizong Li, Penghao Dong, Hantang Qin, and Shanshan Yao\**

The rapid advancements in artificial intelligence, particularly in the domains of robotics, prosthetics, and virtual and augmented reality (VR/AR), have driven an escalating demand for intuitive and effective human-machine interactions. Consequently, haptic devices, being electronic displays for the sense of touch, have drawn increasing attention. More efforts are in demand to develop stretchable and lightweight haptic devices that can trigger multiple mechanical cutaneous receptors using a single device. This work presents a new 3-modal 5-DOF stretchable haptic interface that is enabled by electromagnetic actuators and high-fidelity multi-layer metal printing. The haptic device renders rich haptic sensations (i.e., normal force, vibration, angular force, skin dragging) in one device, allowing for the comprehensive delivery of tactile information through the excitation of multiple cutaneous receptors. Additionally, haptic devices are designed to be compact, lightweight, and skin-compatible. The skin-like softness and stretchability enable intimate skin contact, which is crucial for efficient haptic information delivery. This feature prevents the impediment to natural movements of the skin and ensures the functional integrity of the device during daily deformations of the skin. Finally, three proof-of-concept demonstrations illustrate the potential of the reported multimodal haptic devices for advanced haptic interactions across various domains.

## 1. Introduction

Intuitive and effective human-machine interfaces (HMIs) play a pivotal role in artificial intelligence, spanning from robotics and

rehabilitation to remote operations, smart manufacturing, entertainment, and virtual and augmented reality (VR/AR) (Figure 1a).<sup>[1–6]</sup> Such interfaces have predominantly depended on visual and auditory feedback, as well as conventional control interfaces, such as mice, keyboards, touchpads, and joysticks.<sup>[7]</sup> Tactile perception, exploiting humans' subtle and complex sense of touch, remains underutilized due to the lack of efficient skin-compatible transducers to generate dynamic mechanical stimuli on the skin.

The skin, being the largest sensory organ in the human body, serves as a crucial medium for transmitting diverse information to the human sensory system. The tactile sensation is achieved by triggering cutaneous receptors of the skin with various stimuli. For instance, Pacinian corpuscles primarily respond to rapid vibrations, Merkel cells are sensitive to pressure, and Ruffini endings are in response to skin stretch.<sup>[8–11]</sup> Conventional haptic devices often employ a single actuation mode, with vibration being the most commonly used stimuli. While vibration

has been investigated for delivering haptic information regarding surface roughness through the application of different frequencies,<sup>[12]</sup> vibratory actuators are ineffective in conveying detailed information about shape and surface structure.<sup>[13–16]</sup>

To address the limitations of the conventional actuators and provide users with rich tactile sensations, tactile interactions in rotational shear mode have been explored, where the rotational movement of a tacter is employed to stimulate cutaneous receptors.<sup>[10,11,14,17–19]</sup> Pneumatic/hydraulic actuators and servo motors have been widely explored to exert a rotational shear force.<sup>[20–22]</sup> Rotation shear force could generate haptic sensations that carry angular information from 3D solid surfaces, such as the edge angle and corner angle of an object. Though effective, the presence of heavy supply devices compromises pneumatic/hydraulic actuators' overall portability and compactness.<sup>[23–25]</sup> Servo motors share a common disadvantage of being bulky and rigid.<sup>[14,18,19,26,27]</sup> Dielectric Elastomer Actuators (DEA) have emerged as a promising alternative.<sup>[28,29]</sup> By using soft polymeric materials, DEA-based haptic devices possess excellent flexibility and portability. However, they require high voltages

S. Chen, Y. Li, P. Dong, S. Yao  
 Department of Mechanical Engineering  
 Stony Brook University  
 Stony Brook, NY 11794, USA  
 E-mail: [Shanshan.Yao@stonybrook.edu](mailto:Shanshan.Yao@stonybrook.edu)

L. Yu, W. Shen, H. Qin  
 Industrial and Systems Engineering  
 University of Wisconsin-Madison  
 Madison, WI 53706, USA

B. Fong  
 Department of Electrical and Computer Engineering  
 Stony Brook University  
 Stony Brook, NY 11794, USA

 The ORCID identification number(s) for the author(s) of this article can be found under <https://doi.org/10.1002/adfm.202314515>

DOI: 10.1002/adfm.202314515

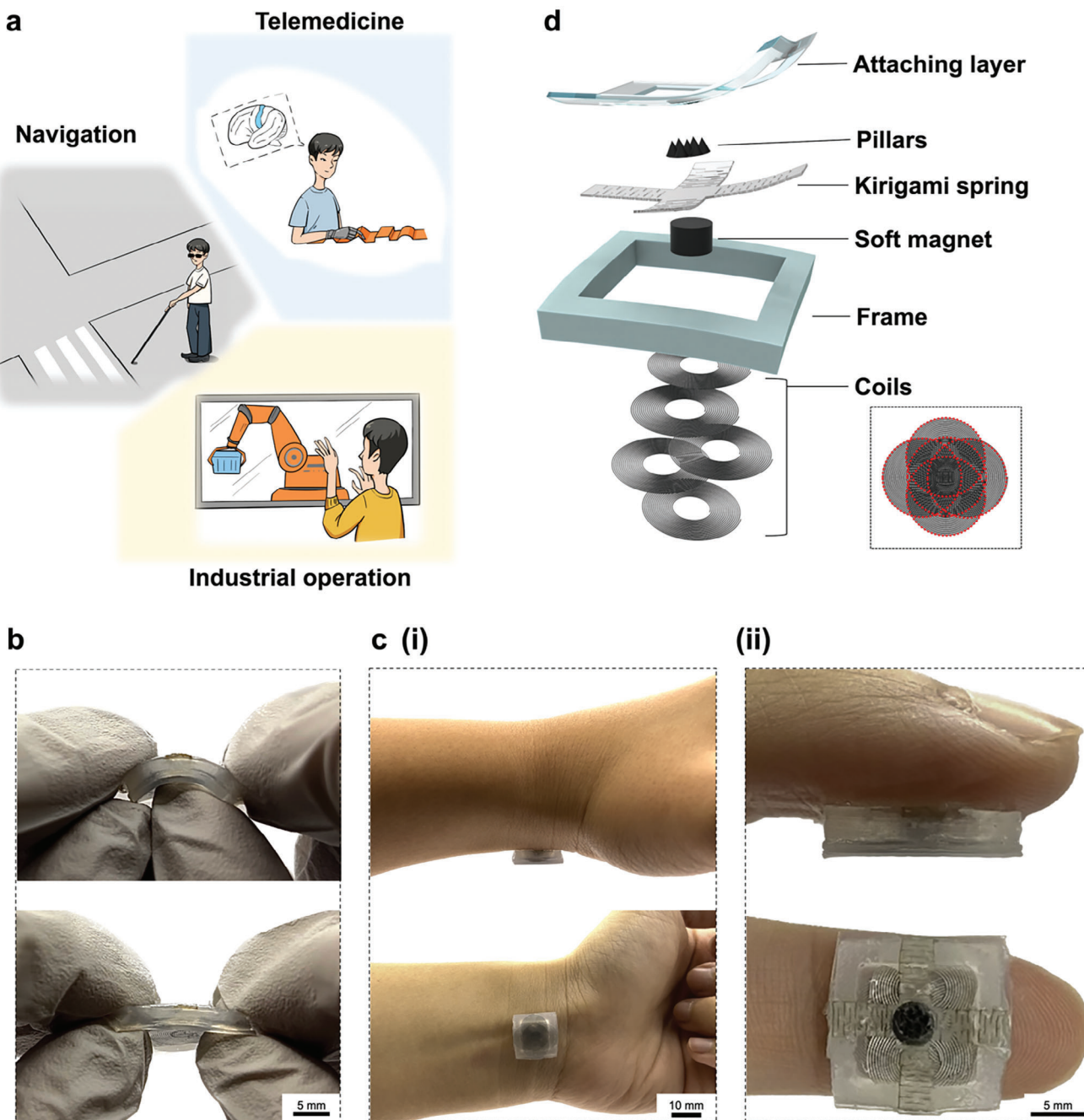


**Figure 1.** Overview of the skin-integrated soft magnetic haptic devices. a) Examples of application scenarios of the device. b) Photographs of the developed soft haptic devices under bending (top) and stretching (bottom). c) Photographs of the haptic device attached to the i) wrist and ii) fingertip. The top images illustrate the side view of the device. The bottom image in (i) shows the bottom view of the device. The bottom image in (ii) shows the top view of the device (the device will be flipped with the soft magnet facing inward during real applications). d) Exploded-view schematic illustration of the device. The insert shows the top view of five coils.

(up to kilovolts) for actuation and can only achieve limited displacement.

In addition to the tactile interactions based on normal pressure/vibration and rotational shear, skin dragging is highly effective in delivering directional cues.<sup>[15,23,30–34]</sup> Existing research typically employs large-area vibration actuator arrays and sequentially triggers each actuator in different skin locations to create

directional patterns.<sup>[35–38]</sup> These devices rely on a complex control system and a large placement space while providing one single degree of freedom (DOF) in the normal mode motion. Only a few haptic devices have demonstrated haptic sensations in both skin dragging and normal mode. For instance, a haptic device based on electromagnetic actuation achieved both haptic sensations, but the haptic interactions are limited to 2-DOF.<sup>[11]</sup>

Recent research efforts have been devoted to exploring a 5-DoF actuator using shape memory alloys (SMA).<sup>[29]</sup> However, the SMA-based actuation mechanism faces challenges in terms of response time and efficiency due to the prolonged heating/cooling time. Moreover, except for DEA-based devices, other haptic interfaces fail to match the stretchability of the skin. Previous user studies have revealed that devices without stretchability have led to poor efficiency in haptic interactions as well as unsatisfied user experiences.<sup>[11,24,39]</sup> Skin-like stretchability and softness are essential to minimize the influence on the user's intuitive actions, improve the mechanical robustness of the device during daily skin deformations, and more importantly, ensure intimate skin contact for precise delivery of mechanical stimuli.

As shown in Table S1 (Supporting Information), there remains a notable gap in the development of stretchable and lightweight haptic interfaces that can trigger multiple mechanical cutaneous receptors through one single device. To fill in the gaps in multi-modal and skin-compatible haptic interfaces, this work presents a new multimodal stretchable haptic interface based on electromagnetic actuators (Figure 1b,c). The actuator provides 3-modal and 5-DOF haptic interactions in one device: Normal mode (1-DOF linear motion along the z-axis), rotational shear mode (2-DOF angular motion around the x-axis and y-axis), and dragging mode (2-DOF linear motion along the x-axis and y-axis). The actuator's strategic 5-DOF movements enable the excitation of multiple cutaneous receptors (e.g., Pacinian, Merkel, and Ruffini) for more comprehensive haptic sensations. The electromagnetic actuator is optimized to provide sufficient stimuli, beyond the human tactile perception threshold. In addition, a novel electric-field facilitated printing method is employed to achieve high-fidelity and multi-layer printing of soft metallic materials into electromagnetic coils. Owing to the optimized structural design and excellent mechanical properties of the employed materials, the reported device is lightweight, compact, and able to maintain functionality for a tensile strain compatible with the elastic properties of the skin.<sup>[40,41]</sup>

## 2. Results

### 2.1. Materials and Structures of Soft Electromagnetic Actuators

The essential part of the haptic device is an electromagnetic actuator (Figure 1d), consisting of five planar spiral coils (used as electromagnetic inductors) and a soft magnet (a composite with magnetic particles dispersed in a polymer matrix). When current passes through the coils, the generated magnetic field enables a multi-modal actuation of the soft magnet. The movement of the soft magnet then generates a multi-modal tactile sensation on the skin. A Kirigami spring is introduced to provide a resistant force to the soft magnet, which prevents the magnet from flipping when subjected to magnetic force and helps the magnet restore its position to the center of the device when coils are de-energized. Additionally, self-assembled pillars are introduced to improve the normal pressure and sliding friction applied onto the skin during actuation. The above components are integrated using a soft frame that provides structural support to the haptic device. Moreover, a thin and skin-safe silicone adhesive layer is added to the top surface of the frame to enable secure and repetitive attachment on the skin.

### 2.2. Multi-Modal Actuation of Soft Electromagnetic Actuators

As illustrated in Figure 2a, the actuator allows for three modes of motion: normal, rotational shear, and dragging. These three modes are capable of stimulating their corresponding cutaneous receptors to generate various haptic sensations. For instance, Merkel disks can be stimulated by normal and rotational pressure/force provided in normal and rotational shear modes. Pacinian corpuscles can be stimulated by vibration provided in the normal mode. Ruffini organs can be stimulated by directional skin stretch provided in the dragging mode. The soft magnet could be actuated with different motions based on the current direction applied to the energized coil and its relative position to the energized coil (Figure 2b). Since the distribution of coils is the same along the x-axis and the y-axis, only coils distributed along the y-axis are shown. In this work, only the working status where the soft magnet is located above the coils is considered. Optical images presenting the movement of the magnet in three working modes are shown in Figure S1 (Supporting Information), and the video is shown in Movie S1 (Supporting Information).

In the interaction between the energized coil and the soft magnet, the current-carrying coil generates a magnetic field, which interacts with the magnetic field of the soft magnet, resulting in a force ( $F_{\text{mag}} \in \mathbb{R}^3$ ) experienced by the soft magnet:<sup>[42]</sup>

$$F_{\text{mag}} = V_r (\mathbf{M} \cdot \nabla) \mathbf{B}_{\text{coil}}(x, y, z) \quad (1)$$

where  $F_{\text{mag}}$  is the magnetic force produced by the coil,  $V_r$  is the volume of the soft magnet,  $\mathbf{M}$  is the magnetization of the soft magnet ( $\mathbf{M} \in \mathbb{R}^3$ ), and  $\mathbf{B}_{\text{coil}}(x, y, z)$  is the magnetic flux density produced by the current-carrying coil ( $\mathbf{B}_{\text{coil}} \in \mathbb{R}^3$ ).

According to the Biot-Savart law, the magnetic flux density produced by the single loop coil can be calculated as follows:

$$\mathbf{B}_{\text{coil}} = \frac{\mu_0}{4\pi} \int_C \frac{Idl \times \mathbf{r}'}{|\mathbf{r}'|^3} \quad (2)$$

where  $\mu_0$  is the vacuum permeability,  $C$  represents the loop,  $I$  is the current applied to the coil,  $\mathbf{r}'$  is the displacement vector ( $\mathbf{r}' \in \mathbb{R}^3$ ) from the current element  $Idl$  to any point on the loop ( $\mathbf{l} \in \mathbb{R}^3$ ).<sup>[43,44]</sup>

The magnetic field generated by the multi-loop coil is explained in detail in Supporting Information (Figure S2, Supporting Information). A microscopic illustration of a soft magnet is shown in Figure S3 (Supporting Information).<sup>[45]</sup> Since the magnetic field generated by the planar spiral coil is symmetrical, the  $y$ - $z$  plane is selected for the explanation. Only the clockwise rotation around the x-axis ( $+\Delta\theta_x$ ) in the rotational shear mode and the linear movement along the positive  $y$ -axis ( $+\Delta y$ ) in the dragging mode are used as examples to explain the actuation mechanisms.

In the normal mode (Figure 2c(i)), the center coil is energized by a counterclockwise current. The force that the soft magnet experienced can be analyzed as:

$$F_{\text{mag}} + F_{\text{spr1}} + F_{\text{spr2}} + F_{\text{skin\_normal}} + N_{c-m} + G = m \cdot \ddot{s} \quad (3)$$

$$F_{\text{spr}} = k \cdot s \quad (4)$$

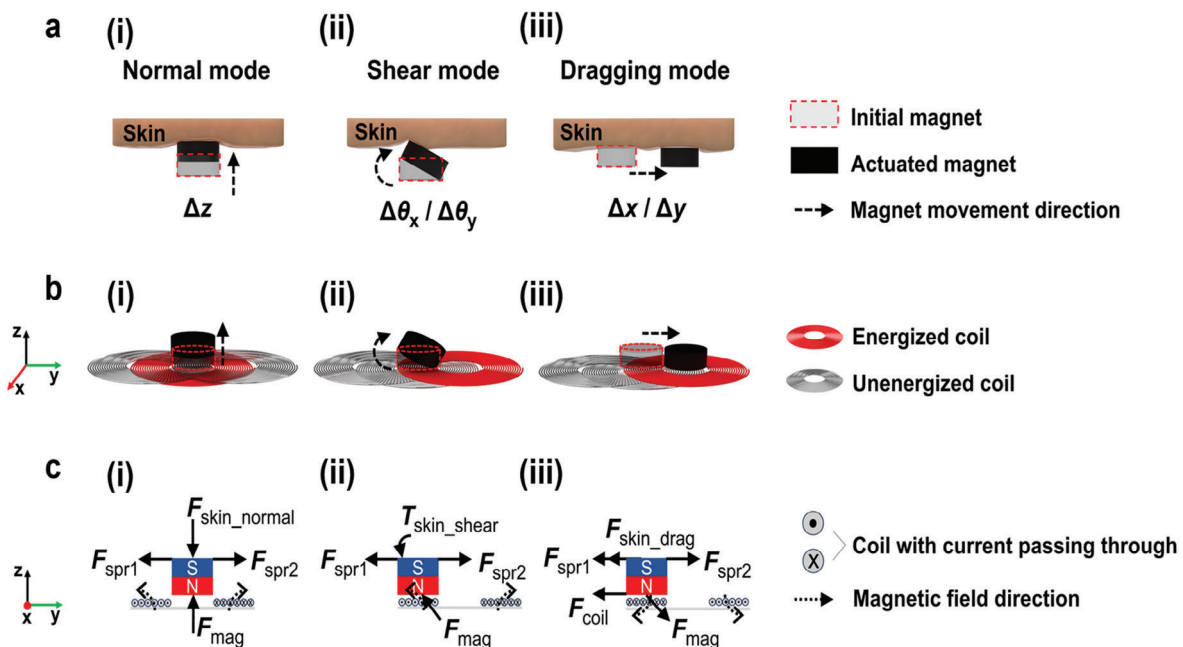


**Figure 2.** Three working modes of soft magnetic actuators. a) Illustrations showing interactions between the actuator and i) the skin under normal mode, ii) rotational shear mode, and iii) dragging mode. “Initial magnet” indicates the position of the magnet when the coil is not energized. “Actuated magnet” indicates the position of the magnet when the coil is energized. b) Working principles of i) the actuator under normal mode, ii) rotational shear mode, and iii) dragging mode. The illustrations only show the magnet and coils along the y-axis; other parts are hidden for clarity. c) Force analysis diagrams of i) the actuator under normal mode, ii) rotational shear mode, and iii) dragging mode. The illustrations only show the magnet and the energized coil; other parts are hidden. The magnets are at the initial position. The diagrams illustrate the forces experienced by the magnet at the moment when the coil is just energized. The support force induced by the coil to the magnet and the gravitational force of the magnet are hidden for clarity.

where  $m$  is the mass of the soft magnet,  $s$  is the displacement of the soft magnet from the initial position ( $s \in \mathbb{R}^3$ ),  $F_{\text{skin\_normal}}$  is the resistant force induced by the skin,  $N_{\text{c-m}}$  is the support force induced by the coil,  $G$  is the gravitational force ( $N_{\text{c-m}}, G \in \mathbb{R}^3$ , they are hidden in the schematic illustrations for clarity),  $F_{\text{spr1}}$  and  $F_{\text{spr2}}$  indicate the resistance from the Kirigami spring ( $F_{\text{spr1}}, F_{\text{spr2}} \in \mathbb{R}^3$ ),  $k$  is the spring constant of the Kirigami structure.

Since the magnet is located at the center of the energized coil initially, resistances from the Kirigami springs are equal and balanced in the  $y$ -axis. The magnetic field provides the magnet with a repulsive magnetic force along the  $z$ -axis. When the current flowing through the coil is large enough, the magnet exhibits a linear motion along the  $z$ -axis ( $+\Delta z$ ). Based on Newton's Third Law of Motion, in the normal mode, the force ( $F_{\text{normal}} \in \mathbb{R}^3$ ) that the actuator could provide to the skin can be calculated as:

$$F_{\text{normal}} = -F_{\text{skin_normal}} \quad (5)$$

In the rotational shear mode (Figure 2c(ii)), the right coil is energized by a counterclockwise current. The force that the soft magnet experienced can be expressed as:

$$F_{\text{mag}} + F_{\text{spr1}} + F_{\text{spr2}} + T_{\text{skin_shear}} + N_{\text{c-m}} + G = m \cdot \ddot{s} \quad (6)$$

where  $T_{\text{skin_shear}}$  ( $T_{\text{skin_shear}} \in \mathbb{R}^3$ ) indicates the torque induced by the skin.

The magnet is located at the left part of the energized coil initially. Based on the Equations (1) and (2), the magnet experiences a repulsive magnetic field force oriented at an angle to the  $z$ -axis. When the current flowing through the coil is large enough,  $F_{\text{mag}}$  will become larger than the total resistance force from all external sources. Then the resultant force provides a torque to rotate the soft magnet. Consequently, the soft magnet undergoes a net force with an angle to the  $z$ -axis that leads to a clockwise rotation around the  $x$ -axis ( $+\Delta\theta_x$ ). In rotational shear mode, the torque ( $T_{\text{shear}} \in \mathbb{R}^3$ ) that the actuator could provide to the skin can be converted as:

$$T_{\text{shear}} = -T_{\text{skin_shear}} \quad (7)$$

In the dragging mode (Figure 2c(iii)), the right coil is energized by a clockwise current. The force experienced by the magnet can be analyzed as:

$$F_{\text{mag}} + F_{\text{coil}} + F_{\text{spr}} + F_{\text{skin_drag}} + N_{\text{c-m}} + G = m \cdot \ddot{s} \quad (8)$$

where  $F_{\text{coil}}$  is the friction induced by the soft magnet/coil interface ( $F_{\text{coil}} \in \mathbb{R}^3$ ), and its direction opposes the motion of the soft magnet. The magnitude of  $F_{\text{coil}}$  can be calculated as<sup>[46]</sup>

$$F_{\text{coil}} = \mu_{\text{c-m}} \cdot N_{\text{c-m}} \quad (9)$$

where  $\mu_{\text{c-m}}$  is the coefficient of friction at the soft magnet/coil interface.  $F_{\text{skin_drag}}$  is the friction induced by the human skin/soft

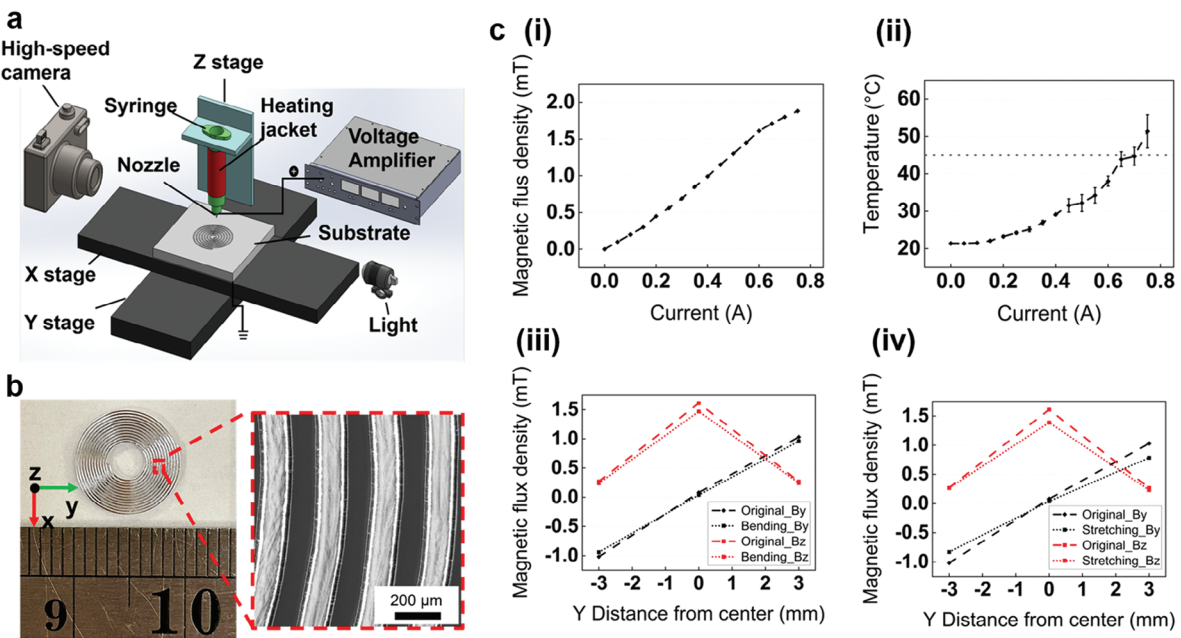


**Figure 3.** Schematics of EADIW and performance of the printed coil. a) Schematic illustration of the EADIW equipment setup. b) Optical images of a printed coil. The insert shows the microscopic image of the coil. c) Magnetic flux density (at the center) of i) the coil with different currents applied. ii) Temperature of the coil with different currents applied. The temperature was measured on the surface of the coils after encapsulated with Ecoflex0030. Magnetic flux density at different locations of the coil when the coil is under the original state (undeformed), iii) bending with an angle of  $\approx 40^\circ$ , and iv) stretching (with  $\approx 15\%$  tensile strain). 0.6 A current was applied during the testing. The coordinate origin is at the center of the coil.

magnet interface ( $F_{\text{skin\_drag}} \in \mathbb{R}^3$ ), and its direction opposes the motion of the soft magnet. The magnitude of  $F_{\text{skin\_drag}}$  can be calculated as

$$F_{\text{skin\_drag}} = \mu_{s-m} \cdot N_{s-m} \quad (10)$$

where  $\mu_{s-m}$  is the coefficient of the friction at the human skin/soft magnet interface,  $N_{s-m}$  is the normal force between the magnet and the skin, and its direction is perpendicular to the skin.

Since the magnet moves from the coil's left part to the center, only the left spring extends and provides resistance. Based on Equations (1) and (2), the magnet experiences an attractive magnetic field force. When the current flowing through the coil is large enough,  $F_{\text{mag}}$  along the  $y$ -axis is larger than the total force from the coil ( $F_{\text{coil}}$ ), the skin ( $F_{\text{skin\_drag}}$ ), and the spring ( $F_{\text{spr}}$ ). The resultant force attracts the magnet toward the energized coil's central axis. Therefore, the magnet exhibits a linear motion along the  $y$ -axis ( $+\Delta y$ ). Thus, in the dragging mode, the force ( $F_{\text{drag}} \in \mathbb{R}^3$ ) that the actuator could provide to human skin can be converted as:

$$F_{\text{drag}} = -F_{\text{skin\_drag}} \quad (11)$$

### 2.3. Characterization and Optimization of Soft Electromagnetic Actuators

#### 2.3.1. Printed Coils

Electric field assisted direct ink writing (EADIW) was employed to fabricate coils (Figure 3a,b). EADIW is capable of printing patterns with high fidelity.<sup>[47]</sup> The application of an electric field

in the EADIW process reduces the existing material size, improves the printing resolution, and ensures the continuity and consistency of the printed patterns. Field's Metal was selected as the conductive material for the coil due to its excellent printability, electrical conductivity, and flexibility.<sup>[48]</sup> The presence of an electric field is vital for the printing quality since the absence of electrostatic attraction between the metal ink and substrate will lead to printing discontinuity and inconsistency in the printed line width.<sup>[47]</sup> Within a commonly used voltage ranging from 0.5 to 2 V (1000 to 4000 V after magnification), the printing quality and line width are not sensitive to the variation in voltage (Figure S4, Supporting Information). The detailed fabrication process is shown in the Experimental Section section. To achieve a large actuation force, the magnetic flux density  $B_{\text{coil}}$  should be optimized (Equation (2)) by adjusting its radius ( $R$ ), number of turns ( $n$ ), and applied current ( $I$ ). As shown in Figure S5 (Supporting Information), a coil with a smaller radius and a larger number of turns will generate a larger magnetic flux density. Considering the range of displacement of the soft magnet in the dragging mode and the printing capability, the linewidth, line spacing, and number of turns of the coil were optimized to be  $\approx 150 \mu\text{m}$ ,  $100 \mu\text{m}$ , and 12 turns, respectively. The coils were printed into two layers to enhance the magnetic flux density  $B_{\text{coil}}$ . These parameters ensure a low coil resistance, less electric heat generated during actuation, and reliable printing quality. The resulting resistance was  $\approx 6 \Omega$  and the current capacity was  $\approx 0.8 \text{ A}$ .

As predicted in Equation (2), the coil generated a higher magnetic flux density with a higher current applied (Figure 3c(i)). Although the coils would not be directly attached to the skin, the temperature generated by the coil should be below  $45^\circ\text{C}$ , to

prevent causing pain sensation if the user accidentally makes skin contact with the coil.<sup>[49]</sup> Therefore, 0.6 A was chosen as a working current (Figure 3c(ii)). Temperature changes of the coil over time are shown in Figure S6 (Supporting Information). It took  $\approx$ 20 s to reach 45 °C. A detailed distribution of  $B_y$  (the magnetic flux density along the y-axis) and  $B_z$  (the magnetic flux density along the z-axis) in the y-z plane generated by the coil are shown in Figure S7 (Supporting Information). To verify the coil's flexibility and stretchability, the magnetic flux density generated by the coil was measured when the coil was subjected to bending and stretching. As illustrated in Figure 3c(iii,iv), the magnetic flux density exhibited slight variations when the coil was bent (with an angle of  $\approx$ 40° to match the curvature of the fingertip) and stretched (with  $\approx$ 15% tensile strain to match the elastic range of the skin). A detailed analysis of the stretchability of the coil and the device can be found in Supporting Information (Figure S8, Supporting Information).

### 2.3.2. Soft Magnet

Based on Maxwell's equations, the correlation between the magnetization  $M$  and the magnetic flux density of the soft magnet ( $B_{\text{mag}} \in \mathbb{R}^3$ ) is

$$M = \frac{\chi}{1 + \chi} \cdot \frac{B_{\text{mag}}}{\mu_0} \quad (12)$$

where  $\chi$  indicates the volume magnetic susceptibility and  $\mu_0$  is the vacuum permeability.

From Equation (12), increasing the magnetic flux density ( $B_{\text{mag}}$ ) of the soft magnet increases the magnetization and positively influences the magnetic field force (Equation (1)), given the predetermined  $B_{\text{coil}}$ . Since the soft magnet is magnetized along the z-axis,  $B_{\text{mag}}$  is approximated as  $B_{\text{mag}}$  (along the z-axis).

Since our device requires a strong remnant magnetic field to interact with the external magnetic field and to form the soft magnet, we chose a hard magnetic material Neodymium Iron Boron (NdFeB) as the magnetic fillers for the soft magnet.<sup>[11,50–53]</sup> For the matrix material, the material should be able to accommodate a high loading of NdFeB while retaining softness, which is vital for the comfortable interactions of the soft magnet with the skin. Among commonly used materials (Figure S9a, Supporting Information), Ecoflex0030 could not accommodate a high NdFeB concentration and the NdFeB/Ecoflex composite became friable at a high loading of NdFeB (8 : 1 in weight ratio). Silicone adhesive and polydimethylsiloxane (PDMS) exhibited a high loading capacity of NdFeB. However, at a high NdFeB concentration (8:1 in weight ratio), the NdFeB/PDMS composite was too rigid (with a modulus of  $\approx$ 72 MPa) and the NdFeB/silicone adhesive composite could not form a self-standing structure. To have a balanced mechanical property, we chose to use a mixture of silicone adhesive and PDMS with a weight ratio of 4 : 1 (named Polymer). This mixture is able to accommodate a large amount of NdFeB to ensure a sufficient magnetic flux density. At the same time, the mixture is soft enough to enable a low modulus of the resulting soft magnet. The detailed fabrication process of the soft magnet is shown in the Experimental Section. It is found that the magnetic flux density ( $B_{\text{mag}}$ ) increases with the NdFeB concentration increase (Figure S9b, Supporting Information). However, when

the concentration is beyond 8 : 1, the soft magnet becomes friable. The elastic modulus of the sample with the concentration of 8 : 1 is  $\approx$ 5 MPa (Figure S9c, Supporting Information), which would be comfortable for interactions with the skin compared with a rigid factor.<sup>[11]</sup> Therefore, NdFeB and polymer weight ratio of 8:1 was chosen to fabricate the soft magnet, resulting in a  $B_{\text{mag}}$  of  $\approx$ 58 mT.

### 2.3.3. Kirigami Springs

The spring should possess a minimal spring constant to avoid negative impacts on the movement of the soft magnet. At the same time, the spring should provide sufficient resistance to prevent the magnet from flipping and ensure the restoration of the soft magnet when the coil current is turned off. Ecoflex0030 was selected as the material for the spring due to its low elastic modulus (Figure S10, Supporting Information). For the springs made by PDMS and thermoplastic polyurethane (TPU), the resistance was too high to enable movement of the soft magnet. Kirigami structures were introduced to further reduce the spring constant. Springs with three common Kirigami patterns, namely Island, Serial, and Parallel (Figure 4a(i)), were fabricated by laser cutting.<sup>[54–56]</sup> The spring with the serial pattern exhibited the lowest spring constant (Figure 4a(ii)). Based on the serial Kirigami pattern, we further optimized the spring constant by tailoring its cutting parameters, as presented in Figure 4b. It was found that springs with smaller thickness possessed a lower spring constant. However, the spring with the lowest thickness (40  $\mu\text{m}$ ) led to self-adhesion, owing to its high surface energy.<sup>[43]</sup> Thus, 80  $\mu\text{m}$  was selected as the optimal thickness for subsequent parameter optimization. Considering the cut length has a greater influence on the spring constant compared to other spring parameters (Figure S11, Supporting Information), this parameter was optimized first. The experimental results demonstrate that the spring constant decreased with increased cut length. Keeping the same cut length at 2 mm, a decrease in spring constant was observed when the cut spacing was reduced. However, when the cut spacing was reduced to 0.25 mm, the spring could not provide sufficient resistance. Hence, a cut spacing of 0.5 mm was deemed optimal. A smaller hinge length (0.5 mm) was selected, resulting in a lower spring constant. For the same hinge length of 0.5 mm, the results indicated that a larger cut width further reduced the spring constant. However, the spring with a cut width of 300  $\mu\text{m}$  was unable to provide sufficient resistance for the soft magnet to work at the expected positions. As a result, 20  $\mu\text{m}$  was selected as the desired cut width. From the above experimental results, the final optimized configuration for the spring is as follows: serial Kirigami pattern, thickness of 80  $\mu\text{m}$ , cutting length of 2 mm, cutting spacing of 0.5 mm, hinge length of 0.5 mm, and cut width of 20  $\mu\text{m}$ .

### 2.3.4. The Skin Contact Surface

Based on Equation (10), to enhance the dragging force  $F_{\text{skin\_drag}}$  from the soft magnet applied to the skin, the coefficient of friction ( $\mu_{s-m}$ ) should be increased. Here, pillar structures are utilized to increase  $\mu_{s-m}$ . Following our previous work, a scalable magnetic field-assisted self-assembly process was used to fabricate

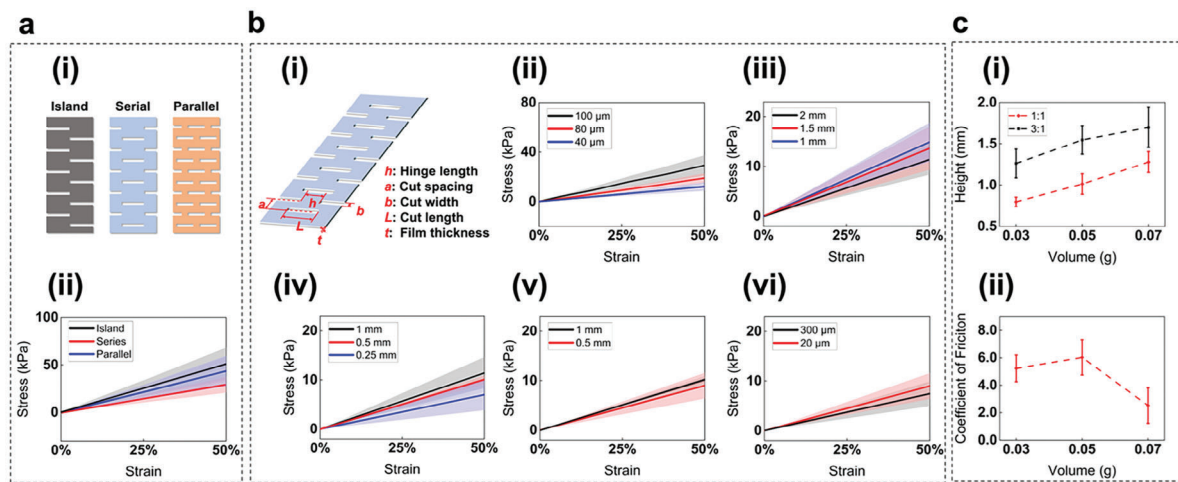


**Figure 4.** Optimization of Kirigami springs and pillars. a) Schematic illustration of different Kirigami patterns (i). Stress-strain curves of springs with different Kirigami patterns (ii). b) Schematic illustration of Kirigami parameters (i). Strain and stress curves of serial patterns with different i) film thickness, iii) cut length, iv) cut spacing, v) hinge length, vi) and cut width. c) Height of the pillars made with different NdFeB: PDMS weight ratios and mixture volumes (i). Coefficient of friction of the devices made from different mixture volumes (ii).

pillars.<sup>[57]</sup> PDMS was used as the liquid precursor and mixed with varying NdFeB weight ratios. To minimize the added thickness to the device, the pillars should have a low height and provide a large coefficient of friction. The geometry of the pillar and the resulting surface coefficient of friction can be tuned by adjusting the NdFeB weight ratio in the PDMS liquid precursor and the volume of the mixture (NdFeB and PDMS), as experimentally illustrated in Figures 4c and S12 (Supporting Information).<sup>[57]</sup> As shown in Figure 4c(i), both the NdFeB weight ratio and the volume of the mixture positively influence the pillars' height. To achieve a smaller height of the device, a lower NdFeB: PDMS weight ratio of 1:1 was selected. Based on our prior research, the elastic modulus of PDMS : NdFeB with a weight ratio of 1 : 1 is  $\approx 1$  MPa, which could improve haptic sensation without penetrating the human skin.<sup>[57]</sup> When the volume of the mixture increased from 0.03 g to 0.05 g, the surface coefficient of friction increased (Figure 4c(ii)). Further increasing the mixture volume to 0.07 g led to the bending of the pillars due to a larger height. Together with a decreased areal pillar density, the surface coefficient of friction was reduced. A user study was conducted to compare and evaluate the effectiveness of different skin contact surfaces: surfaces without pillars and surfaces with pillars made of various volumes of NdFeB and PDMS mixture. Detailed information regarding the user study is provided in the Experimental Section. The results of the user study show that among all surfaces, the skin contact surface with the pillars made of 0.05 g NdFeB and PDMS mixture provided the most intensive haptic sensation under normal, rotational shear, and dragging mode. Therefore, NdFeB : PDMS ratio of 1 : 1 and the mixture volume of 0.05 g were selected to fabricate the optimal pillar structure.

### 2.3.5. Performance of the Haptic Device

The performance of the haptic device was evaluated in normal, rotational shear, and dragging modes. Prior research has shown that 100 μm of displacement and 15 mN of force were considered as the threshold to trigger tactile perception in the normal

mode.<sup>[58]</sup> Around 0.3 mm of displacement was considered as the threshold for lateral tactile perception.<sup>[11]</sup> Displacement and force (normal and dragging modes) or angle and torque (rotational shear mode) were employed as evaluation metrics, as presented in Figure 5a,b. The force or torque exhibited a positive correlation with the applied current and the resulting magnetic flux density. Under the normal mode, the actuator could generate a maximum force of  $\approx 28$  mN. Under the rotational shear mode, the device could provide a maximum torque of  $\approx 90$  mN·mm. When operated in the dragging mode with the magnet held at the center initially, the device achieved a maximum dragging force of 5 mN. Based on the results of the user study (discussed in the next section), the device could sufficiently trigger the skin's tactile sensations under all three modes.

Similarly, an increase in current led to a larger displacement (in normal and dragging modes) or angle (in the rotational shear mode). When the applied current exceeded 0.2 A, the normal displacement exhibited a significant upward trend, reaching a maximum value of  $\approx 1.8$  mm. In the rotational shear mode, the angular motion induced by electromagnetic forces started to increase beyond a current of 0.25 A and reached 51° at 0.6 A. The dragging displacement followed a similar trend to that of the normal mode. Beyond a current of 0.2 A, the dragging displacement is larger than the required value for triggering tactile sensation (0.3 mm).

The device's performance at dynamic response was then evaluated by applying a current of 0.6 A to the coil at various frequencies (Figure 5c). The actuator demonstrated a stable operation at frequencies below 20 Hz in both normal and rotational shear modes. Despite a decrease in displacement as the frequency exceeded 20 Hz, haptic sensation could still be triggered at frequencies up to  $\approx 200$  Hz. In the dragging mode, the actuator exhibited a favorable performance for frequencies ranging from 1 to 10 Hz. Similarly, although the actuator's performance decreased significantly with further increased frequency, it still surpassed the haptic sensation threshold for frequencies within 80 Hz.

To validate the device's repeatability and cyclic stability in different modes, cyclic testing of 10 000 cycles was performed in

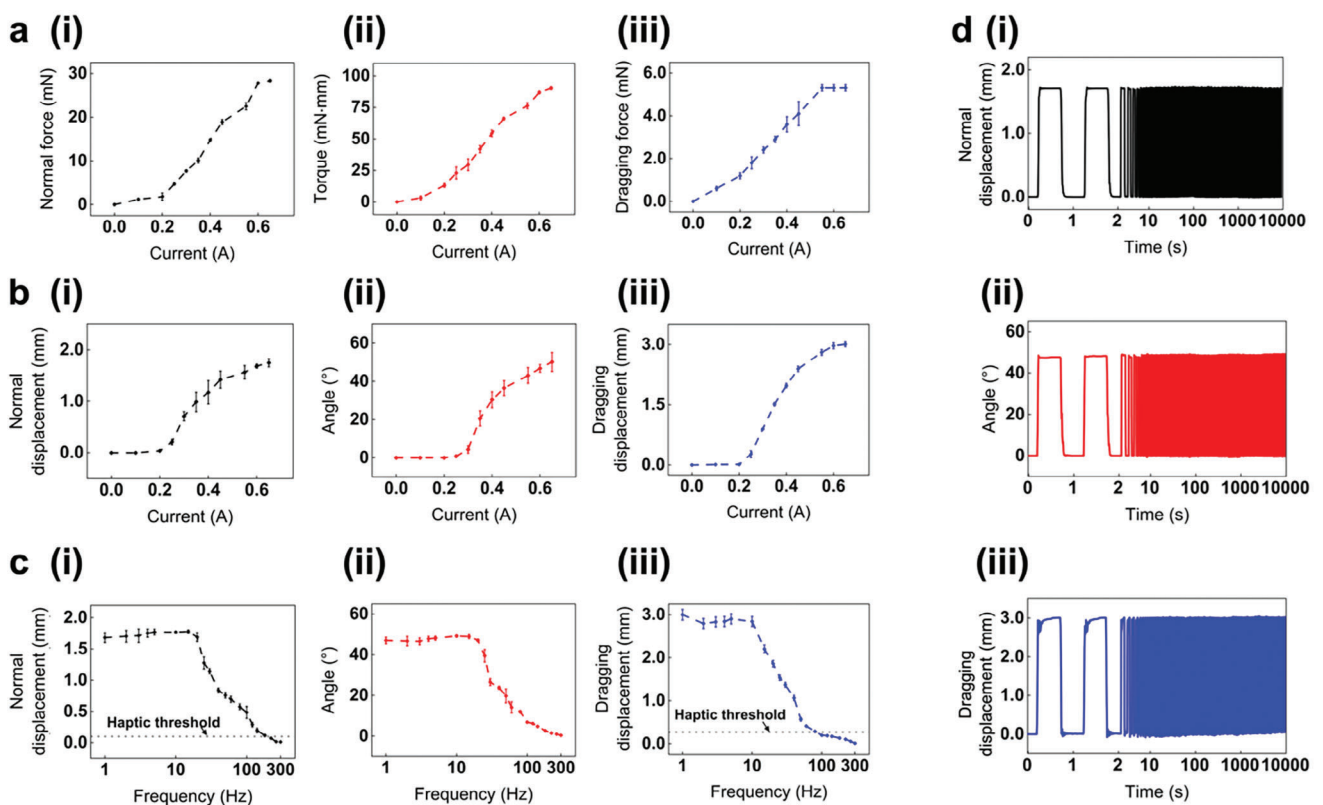


**Figure 5.** Performance of the haptic device under three working modes. a) Force and torque under i) normal mode, ii) rotational shear mode, and iii) dragging mode. b) Displacement and angle under i) normal mode, ii) rotational shear mode, and iii) dragging mode. c) Performance of the actuators at different frequencies under i) normal mode, ii) rotational shear mode, and iii) dragging mode. d) Performance of the actuators during 10000 cycles of operation under i) normal mode, ii) rotational shear mode, and iii) dragging mode. All measurements were performed with a coil current of 0.6 A.

the normal, rotational shear, and dragging modes. As shown in Figure 5d, the device demonstrated excellent stability for all three modes. The response time was  $\approx 30$  ms under normal and rotational shear mode and 100 ms under dragging mode. The flexibility and stretchability of the device were also tested (Figure S13, Supporting Information). Though there was a slight performance reduction when the device was bent or stretched, the device was still able to provide sufficient stimuli to trigger the skin's tactile receptors.

#### 2.4. Proof-Of-Concept Demonstrations

##### 2.4.1. Application of the Normal Mode in Recognition of Different Working Status

In remote industrial operations, haptic devices serve as the interface to provide real-time information regarding the robot's working status to the operators. By this means, the operators are able to make necessary adjustments during operations. In this scenario, the normal mode of the developed haptic device was employed to provide users with indications of the different working statuses of the robot (Figure 6a(i)). As illustrated in Figure 6a(ii), when the robotic arm starts operating by making contact with an object, the actuator delivers a single tapping to the user. When an object is held between robotic arms during a normal working

status, the actuator provides a series of low-frequency tapping to inform the users. In case of an emergency, such as slippage of the object, the actuator provides high-frequency vibrations to alert the user. To assess the effectiveness of the haptic device in transforming working status information, a user study was conducted. The actuator was worn on the user's fingertips in a blindfolded and acoustically shielded setup. In the experiments, the actuator was activated by a current of 0.6 A for 1 s with a 2 s pause (single tapping), at a frequency of 1 Hz (low-frequency tapping), and at a frequency of 100 Hz (high-frequency vibrations). After each activation, the users were asked to identify the received types of tapping/vibration that represent different working statuses. Each working mode was delivered to the users 70 times randomly, resulting in a total of 210 tests. As summarized in Figure 6a(iii), all three working statuses achieved a perception rate of 100%, indicating an excellent transmission of the working status to the users.

##### 2.4.2. Application of the Rotational Shear Mode in Recognition of Angular Information

Recognition of 3D solid surfaces is crucial for our interactions with the surrounding world and for delivering information related to different surfaces. As an example, in scenarios where a patient wears a prosthesis, such haptic feedback can improve the

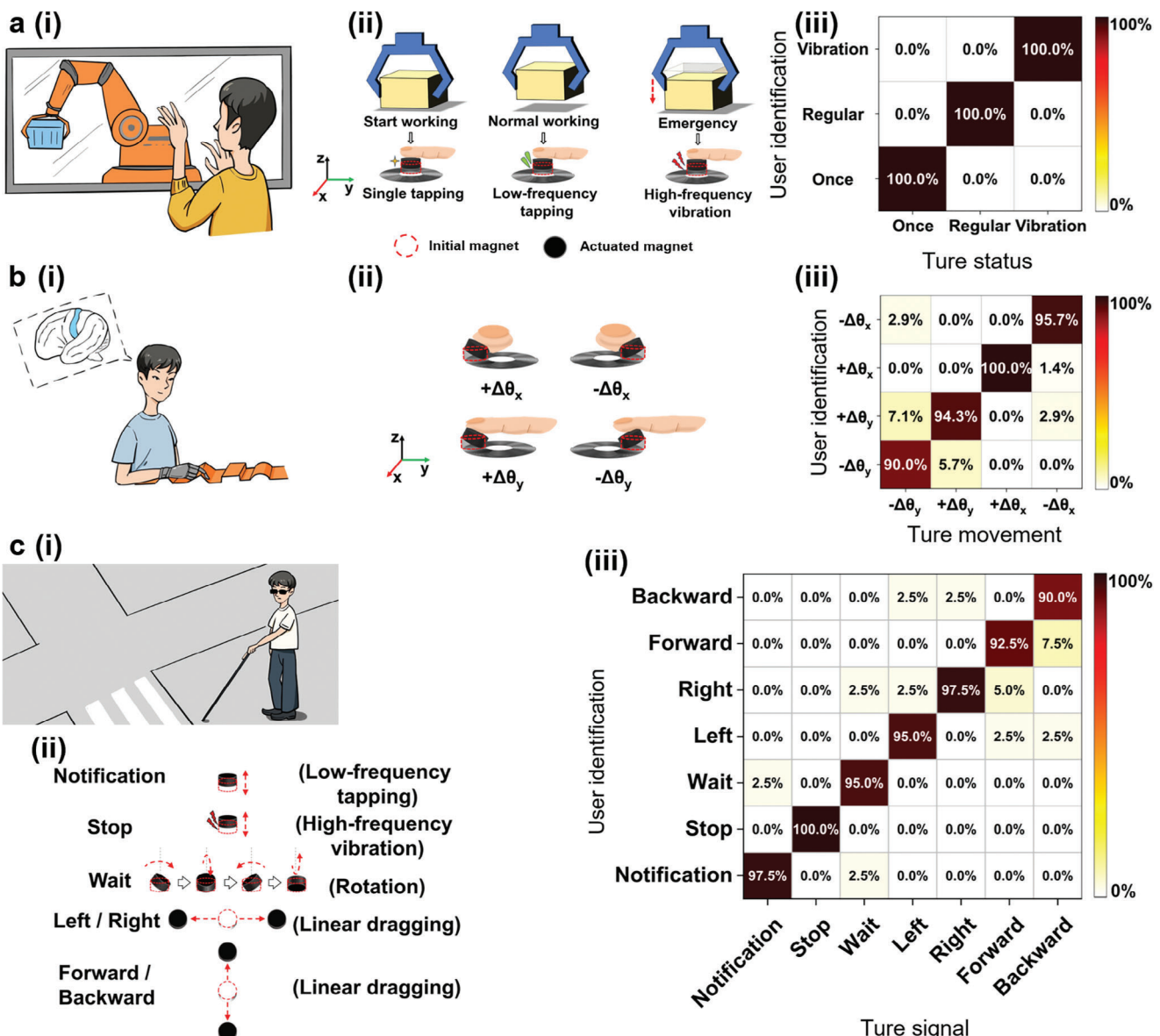


**Figure 6.** Schematic illustrations and results of the user study. a) Application of the normal mode in recognition of different working statuses (i). ii) Schematic illustration of the user study and iii) the corresponding confusion matrix. b) Application of the rotational shear mode in the recognition of angular information (i). ii) Schematic illustration of the user study and iii) the corresponding confusion matrix. c) Application of multimodal haptic interactions in the recognition of different navigation signals (i). ii) Schematic illustration of the user study and iii) the corresponding confusion matrix. Note that the schematic of the device shown in this figure is simplified for clarity purposes. The complete device structure can be found in Figure 1d and Section Assembly under Experimental Section.

patient's control of the prosthesis during physical interactions with the environment, thereby increasing productivity, safety, and comfort. Rotational shear force could generate haptic sensations that carry angular information from 3D solid surfaces, such as the edge angle and corner angle of an object. In our user study, the angular information corresponding to different surface structures was provided by varying the angle between the skin and the contact surface of the actuator and delivered by triggering cutaneous receptors of the skin (Figure 6b(i)). The actuator working in the rotational shear mode was employed to provide the required angular motion. As illustrated in Figure 6b(ii),

the actuator provided tactile sensations in four different angular movements to mimic the condition that fingers were in contact with 3D surfaces with different angles. The experimental setup was similar to that of the working status recognition. The actuator was attached to the fingertip and applied with a current of 0.6 A at the frequency of 1 Hz for 3 s. Four different angular movements were generated by regulating the coil current. Each angular movement was delivered to the users 70 times randomly. The results, summarized in Figure 6b(iii), show that the actuator was able to provide tactile sensations for angular information discrimination, with an average perception rate of 95%.

#### 2.4.3. Application of the Dragging Mode in the Recognition of Different Navigation Signals

Navigation signal recognition, which involves identifying the different notifications and directions of tactile feedback on the skin, is a desired capability in haptic devices (Figure 6c(i)). For instance, providing navigation information through tactile feedback is particularly beneficial for individuals with visual impairments or when the visual sensation is occupied by other tasks (e.g., during driving). In contrast to conventionally employed vibration actuator arrays,<sup>[35–38]</sup> our device achieves directional cues in four directions using one single device through a simple control system and requires a smaller placement space for the actuator. A multimodal and multi-DOF haptic device could enrich the users' tactile experience and reduce the fatigue and desensitization caused by receiving a single tactile signal, thus improving the effectiveness of navigation information transmission.<sup>[25]</sup> To examine the actuator's ability to convey navigation information, the actuator was attached to the wrist for hands-free operation. Seven different navigation signal patterns (i.e., notification, stop, wait, left/right, and forward/backward) (Figure 6c(ii)) were generated by the actuator working in three different working modes. The navigation signal patterns were generated 40 times in a randomized order, resulting in a total of 280 tests. Users were asked to differentiate the navigation signal patterns and the results were summarized in Figure 6c(iii). The user study illustrates an average perception rate of ≈95.4% for different navigation signals.

As shown in Figure S14 (Supporting Information), a user study demonstrates that stimuli provided in three different working modes at a low frequency (1 Hz) can be distinguished with an average perception rate of 96.7%. However, it was difficult for the users to distinguish among three different working modes provided at a high frequency (100 Hz). The experimental details can be found in Experiment Section.

### 3. Conclusion

This work presents a 3-modal 5-DOF wearable electromagnetic actuator for comprehensive haptic information transmission. This multi-modal actuator is capable of satisfying the requirements of tactile perception as well as matching the elastic properties of the skin. A novel printing method was employed to fabricate high-resolution coils with good flexibility and stretchability. With three actuation modes (normal, rotational shear, and dragging), the developed actuator could stimulate multiple cutaneous receptors by providing a force of 28 mN and a displacement of 1.8 mm in the normal mode, a torque of 90 mN·mm and an angle of 51° in the rotational shear mode, and a force of 5 mN and a displacement of 3 mm in the dragging mode. A Kirigami spring was introduced to ensure the actuator's functionality and reliability. With integrated self-assembled pillars, the normal/rotational shear pressure and sliding friction delivered by the actuator could be amplified without increasing the applied current. The user studies demonstrate that the haptic device was able to deliver multi-modal haptic sensation and convey information regarding working status (through vibrations), angular surface structure, and directional signals. These demonstrations highlight the potential applications of the haptic device in human-machine in-

teractions across varying fields, including industrial operation, telemedicine, entertainment, and navigation.

### 4. Experimental Section

**Materials:** PDMS (Dow Sylgard 184) was obtained from Ellsworth Adhesives. Ecoflex0030 and Ecoflex gel were obtained from Smooth-On, Inc. The silicone adhesive (LiveoTM MG 7–9900) was obtained from Knowde. NdFeB magnetic particles were obtained from Magnequench International, LLC. Field's Metal was obtained from Fisher Scientific International, Inc. All materials were used as received.

**Fabrication of Soft Electromagnetic Actuators:** *Coil Fabrication:* The present study employed the EADIW Technique (Figure 3a,b) to fabricate coils utilizing a low melting point alloy, Field's Metal (melting point: 62 °C). The laboratory-built EADIW system comprises several essential components, including the printing syringe, printing nozzle, heating jacket, high-precision stage, waveform generator, voltage amplifier, high-speed camera, and illuminating light. The 3-axis precision stages (Aerotech, ANT130LZS) were controlled by a motion controller (Aerotech, A3200) to position the printing nozzle. Small chunks of the alloy were loaded into the glass printing syringe and mounted onto the syringe holder on the Z-axis precision stage. The program for printing the coil pattern was prewritten with its associated controlling software. A heating jacket (Fisherbrand, FSDS120JC-A) was wrapped around the body of the syringe and the nozzle to melt the alloy inside. The printing nozzle with an ID of 108 µm (Subrex) was fixed on the head of the syringe with a Luer lock. A copper wire was also fixed at the Luer lock, extended out, and connected to the output port of the voltage amplifier to receive electricity. The voltage amplifier (Trek, 610e) was set to magnify the voltage signal 2000 times, which received signal from the waveform generator (Keysight, 33500B) controlled by Keysight BenchVue on a PC for adjustment, activation, and deactivation. An aluminum plate was mounted above the X-Y-axis precision stages and connected to the ground port of the amplifier. A 75 mm (length) x 25 mm (width) x 1 mm (height) glass slide was put above the aluminum plate serving as the substrate for printing. The glass slide was coated with a sacrificial layer of acetone-dissolvable acrylonitrile butadiene styrene (ABS). This layer made it easier to integrally peel off the coils from the glass substrate after printing. The high-speed camera (Chronos, 1.4) assisted by an illuminating light (Stocker, 21DC) was used to monitor the printing process and project its vision on a PC monitor. The lens of the camera was oriented toward the printing position from one side, with a tilted angle of ≈10° above the horizontal plane. The illuminating light with adjustable brightness was shot from the opposite side with a similar tilted angle.

The printing process started with turning on the heating jacket to melt the loaded alloy. During the printing process, control was exerted over the nozzle temperature, ensuring that the temperature remained within the precise range of 90–110 °C to obtain the ideal alloy viscosity. The nozzle was positioned to obtain a standoff distance of ≈60 µm. A few slight knocks were made on the syringe to impel the melted alloy to flow out of the nozzle tip and touch the substrate. The Direct Current mode was used for the signal, with a voltage of 1 V. After the signal was turned on, the printing was started in the Aerotech controlling software. The printing speed was set to be 1 mm s<sup>-1</sup>. The application of an electric field in the EADIW process serves two key functions: First, it supplies surface tension potential energy combined with electric potential energy to reduce the exiting material size. Second, the electric field creates electrostatic attraction, ensuring the printed material adheres consistently to the printing substrate while the voltage was applied. The absence of the electric field significantly diminishes the continuity and consistency of the printed lines. All coils used in this study have been coated with Ecoflex0030 (≈50 µm) to maintain the geometry.

**Soft Magnets:** To accommodate a higher concentration of NdFeB microparticles, a mixture of silicone adhesive and PDMS with a weight ratio of 4:1 (named Polymer) was selected as the polymer matrix material. Then the Polymer was mixed with NdFeB and toluene (Thinky, AR-100) with a weight ratio of 1 : 8 : 2 and poured into a 3D printed mold (20 mm x 20 nm x 5 mm) (Prusa Research, i3 MK3S+). The mixture was degassed for

2 h and thermally cured on the hotplate at 80 °C for 3 h. After curing, the soft magnet was magnetized under a 3.5 T magnetic field (ASC Scientific, IM-10-30). The prepared magnetic composite was cut into a cylinder 3 mm in diameter and 2 mm in height using a sampling punch (WellTech, Rapid-Core-3.0).

**Pillars:** Soft pillars were made by a self-assembly procedure. First, a mixture of PDMS and NdFeB with a weight ratio of 1:1 was prepared. Then, 0.05 g mixture was dropped onto a petri dish and spread evenly. To form the pillars, a NdFeB magnet (K&J Magnetics, DEX2) was placed underneath the petri dish and moved up and downward perpendicularly to the bottom of the petri dish for 10 cm. This procedure was repeated until the mixture was formed into conical pillars. The pillars were preliminarily cured at 75 °C (with a magnet) for 3 h and then fully cured at 150 °C (without a magnet) for 2 h.

**Kirigami Springs:** Kirigami spring was made by Ecoflex0030. 1.2 g mixture of Ecoflex0030 part A and part B with a weight ratio of 1:1 was poured onto a petri dish. To form a thin film, the mixture was spin-coated (Laurill Technologies, WS-650Mz-23NPPB) at 300 rpm for 1 min, followed by thermal curing at 80 °C for 1 h. To achieve the expected Kirigami geometry, the thin film was cut by a laboratory-built picosecond laser cutting system (Photonics Industries, RG20H-532) with a wavelength of 532 nm, pulse repetition rate of 100 kHz, and laser power of 5 W.

**Other Components:** A ring-shaped Ecoflex gel thin film served as the interface layer, which facilitated the adhesion of the device to the skin. A mixture of Ecoflex gel part A and part B (1:1 by weight) was poured onto a ring-shaped mask, followed by thermal curing on the hotplate at 80 °C for 1 h. A ring-shaped frame made by Ecoflex0030 served as a support for the Kirigami spring as well as a bonding medium for the Kirigami spring and coils. A mixture of Ecoflex0030 part A and part B with a weight ratio of 1:1 was poured into a ring-shaped 3D printed mold (Prusa Research, i3 MK3S+). The height of the mold was 3 mm, and the thickness was 2 mm. Then the mold filled with Ecoflex0030 was degassed for 30 min and thermally cured on the hotplate at 80 °C for 1 h.

**Assembly:** Five printed coils were placed as shown in Figure 1d and covered by Ecoflex0030. A frame was placed on the stack of coils and bonded to the substrate of the stack of coils using Ecoflex0030 as the adhesive. A drop of Ecoflex0030 was added at the center of the Kirigami spring followed by placing the soft magnet on top of it. After thermal curing at 60 °C for 30 min, the Kirigami spring, boned with the soft magnet, was placed on the frame using Ecoflex0030 as the adhesive. The soft pillars were cut to fit the shape of the soft magnet using the same sampling punch. A drop of Ecoflex0030 was added at the center of the Kirigami spring followed by placing the soft pillars at the center of the spring. A ring-shaped Ecoflex gel thin film was placed on the frame with Ecoflex0030 as an adhesion material. Finally, the whole device was fully cured at room temperature for 1 h.

**Control System:** A control system was designed to manage the current flow through five coils, thereby controlling the motion of the soft magnet. This system was composed of a microcontroller (Arduino Nano V3), a Salon 8-Channel DPDT Signal Relay Module (D-261 Series Ver. 2.0), and a power supply (Keysight Technologies, E3649A). The magnitude of the current passing through the coils was provided by the power supply. The current was directed from the power supply to a specific coil through one of the eight dual double-pole double-throw (DPDT) switch channels available on the Salon module. The activation and deactivation of the switch and the regulation of the current passing through each coil were controlled by the Arduino Nano. This configuration allowed for the alteration of current direction through the coil simply by flipping the switch, without the need for power and ground reconnections. The schematic illustration with more description and the optical image of the overall working system can be found in the Supporting Information (Figure S15, Supporting Information).

**Characterizations: Strain–Stress Curve Measurements:** Strain–stress curve measurement was conducted using a material testing system (858 Mini Bionix II, MTS). All Kirigami spring samples were cut into 6 mm in length and were applied with 50% strain. The stress values were obtained by dividing the tensile force by the cross-sectional area of the Kirigami springs. The strain values were calculated by dividing the distance by the length of the Kirigami springs.

**Force and Torque Measurements:** The normal force was quantified by measuring the weight lifted by the soft magnet.<sup>[42]</sup> The weight used for both normal force, torque, and dragging force measurements was measured by an analytic balance (Ohaus, PX3202). The weight was added incrementally to the magnet until the magnet could not move along the z-axis. The magnitude of the normal force was equal to the gravitational force of the weight.

The configuration for measuring torque was similar to that of normal force. The weight was added incrementally to the magnet until the soft magnet could no longer induce angular motion. The magnitude of rotational shear force ( $F$ ) is equal to the gravitational force of the weight. The torque ( $T_{\text{shear}}$ ) can be calculated using the following formula:

$$T_{\text{shear}} = r \cdot F \sin \theta \quad (13)$$

where  $r$  is the radius from the axis of rotation to the point of the rotational shear force.  $\theta$  is the angle between  $F$  and the lever arm.

In the dragging force measurement, the magnet was connected to a weight through a laboratory-built pulley system.<sup>[11]</sup> Weight was incrementally increased until the magnet could no longer be securely maintained at the center of the coil. The magnitude of the dragging force is equal to the gravitational force of the weight.

**Other Measurements:** Magnetic flux density was measured by a magnetometer (Metamotions, Mbientlab). Each magnetic flux density measurement was repeated three times. Temperature was measured by a thermometer (Omega Engineering Inc, HH802U). The thermometer was placed on the surface of the coils that were coated with  $\approx 50 \mu\text{m}$  Ecoflex0030 thin film. At each current level, the measurement was repeated three times. All displacements were measured by a laser sensor (Keyence Corporation, IL-S025). Optical images were captured by a camera (Apple, iPhone 14). Microscopic images were obtained by a microscope (Evident, BX53M).

**Comparisons of Haptic Sensation with Different Skin Contact Surface:** One user study was conducted to determine the intensity of haptic sensation delivered on human skin that was given by different skin contact surfaces with various pillars. Four subjects were recruited in this study, with the ratio of male to female of 1:1, ages ranging from 20 to 30 years old. Four types of surface structures were tested in this study, involving one surface of the original soft magnet and three different surfaces reinforced by self-assembled pillars made of different NdFeB and PDMS mixture volumes. The surface of the original soft magnet was named Surface #1; the surface made of 0.03 g, 0.05 g, and 0.07 g mixture of NdFeB and PDMS were named Surfaces #2, #3, and #4, respectively.

This experiment was conducted in a blindfolded and acoustically shielded setup. Four types of surface structures were placed in front of the subjects in a random order. The subjects were asked to perform two motions. Subjects were first asked to vertically press onto each surface with the same finger five times with self-perceived the same amount of gentle force. Pressing onto the surface structures resembles the interaction between the human skin and the actuator in a normal and rotational shear mode. Subjects were then asked to rank the intensities of haptic sensations they received from pressing onto different surfaces in the order of the lowest to the highest. Subjects were then asked to horizontally slide across each type of surface with the same finger five times, with self-perceived the same amount of gentle force. The sliding motion resembles the interaction between the human skin and the actuator working in a dragging mode.

With the completion of the user study, 4/4 subjects ranked Surface #2 as the surface structure that delivered the most intensive haptic sensations and Surface #1 as the least intensive during both pressing and sliding motions. According to the result of this user study, Surface #2 was chosen as the optimized skin contact surface.

**User Study about Distinguishing Among Three Working Modes:** The actuator was worn on the user's fingertips in a blindfolded and acoustically shielded setup. In the experiments, the actuator was activated by a current of 0.6 A at a frequency of 1 Hz (low frequency) or 100 Hz (high frequency). After each activation, the users were asked to identify the received actuator

working mode. At each frequency level, each working mode was delivered to the users 25 times randomly, resulting in a total of 150 tests.

**Statistical Analysis:** The data were expressed as the “mean  $\pm$  standard deviation”. Error bars in all figures are the standard deviations obtained from at least five independent measurements. All the data were analyzed by Excel and plotted by Origin.

## Supporting Information

Supporting Information is available from the Wiley Online Library or from the author.

## Acknowledgements

This material was based upon work supported by the National Science Foundation under Award No. ECCS-2238363. S.Y. would like to acknowledge the support from the start-up fund at Stony Brook University. The authors would like to thank Yiting Zheng, from David J. Jae-Seok Hwang's lab at Stony Brook University, for assisting in laser cutting. The authors would like to thank Lenore Y. Zhao, from the School of Health Professions at Stony Brook University, for providing physiological knowledge about haptic sensations.

## Conflict of Interest

The authors declare no conflict of interest.

## Author Contributions

S.C. and S.Y. conceived the project. L.Y. and W.S. fabricated the printed coils. S.C. fabricated the other parts of the electromagnetic actuators and performed the experiments. B.F. designed and fabricated the control system. S.C. and L.Y. compiled figures. S.C., L.Y., W.S., Y.L., P.D., and S.Y. participated in discussions and data analysis. Finally, S.C., L.Y., and S.Y. wrote the manuscript with contributions from all the authors. S.Y. supervised this project.

## Data Availability Statement

The data that support the findings of this study are available from the corresponding author upon reasonable request.

## Keywords

electromagnetic actuators, multimodal haptic devices, soft actuators, stretchable electronics, wearable electronics

Received: November 17, 2023

Revised: February 8, 2024

Published online: February 22, 2024

- [4] Y. Pang, S. Chen, Y. Cao, Z. Huang, X. Xu, Y. Fang, C. Cao, *Adv. Mater. Interfaces* **2022**, 9, 2201202.
- [5] Y. Pang, X. Xu, S. Chen, Y. Fang, X. Shi, Y. Deng, Z.-L. Wang, C. Cao, *Nano Energy* **2022**, 96, 107137.
- [6] S. Zhang, A. Chhetry, M. A. Zahed, S. Sharma, C. Park, S. Yoon, J. Y. Park, *Npj Flex. Electron.* **2022**, 6, 11.
- [7] M. Zhu, Z. Sun, Z. Zhang, Q. Shi, T. He, H. Liu, T. Chen, C. Lee, *Sci. Adv.* **2020**, 6, eaaz8693.
- [8] X. Ji, X. Liu, V. Cacucciolo, Y. Civet, A. El Haitami, S. Cantin, Y. Perriard, H. Shea, *Adv. Funct. Mater.* **2021**, 31, 2006639.
- [9] J. T. Kim, H.-S. Shin, J.-Y. Yoo, R. Avila, Y. Huang, Y. H. Jung, J. E. Colgate, J. A. Rogers, *Extreme Mech. Lett.* **2023**, 58, 101940.
- [10] K. T. Yoshida, C. M. Nunez, S. R. Williams, A. M. Okamura, M. Luo, presented at 2019 IEEE World Haptics Conf. (WHC), Tokyo, July **2019**.
- [11] L. Fang, T. Zhu, E. Pescara, Y. Huang, Y. Zhou, M. Beigl, in *Augmented Humans 2022*, ACM, Chiba, March **2022**.
- [12] Y. Huang, J. Zhou, P. Ke, X. Guo, C. K. Yiu, K. Yao, S. Cai, D. Li, Y. Zhou, J. Li, T. H. Wong, Y. Liu, L. Li, Y. Gao, X. Huang, H. Li, J. Li, B. Zhang, Z. Chen, H. Zheng, X. Yang, H. Gao, Z. Zhao, X. Guo, E. Song, H. Wu, Z. Wang, Z. Xie, K. Zhu, X. Yu, *Nat. Electron.* **2023**, 6, 1020.
- [13] B. Lim, K. Kim, D. Hwang, presented at 2017 IEEE Int. Conf. Robotics and Biomimetics (ROBIO), Macao, December **2017**.
- [14] H. Benko, C. Holz, M. Sinclair, E. Ofek, presented at 29th Annual Symp. User Interface Software and Technology, Tokyo, October **2016**.
- [15] A. Manasrah, S. Alkhalil, in *Int. Conf. Human Haptic Sensing and Touch Enabled Computer Applications* (Eds: I. Nisky, J. Hartcher-O'Brien, M. Wiertlewski, J. Smeets), Springer International Publishing, Cham, September **2020**.
- [16] X. Yu, Z. Xie, Y. Yu, J. Lee, A. Vazquez Guardado, H. Luan, J. Ruban, X. Ning, A. Akhtar, D. Li, B. Ji, Y. Liu, R. Sun, J. Cao, Q. Huo, Y. Zhong, C. Lee, S. Kim, P. Gutruf, C. Zhang, Y. Xue, Q. Guo, A. Chempakasseril, P. Tian, W. Lu, J. Jeong, Y. Yu, J. Cornman, C. Tan, B. Kim, et al., *Nature* **2019**, 575, 473.
- [17] P. Zhang, M. Kamezaki, Y. Hattori, S. Sugano, presented at 2022 Int. Conf. Robotics and Automation (ICRA), Philadelphia, May **2022**.
- [18] J. Gong, D. Y. Huang, T. Seyed, T. Lin, T. Hou, X. Liu, M. Yang, B. Yang, Y. Zhang, X.-D. Yang, presented at 2018 CHI Conf. Human Factors in Computing Systems, Montreal, April **2018**.
- [19] A. Girard, M. Marchal, F. Gosselin, A. Chabrier, F. Louveau, A. Lécyer, *Front. ICT* **2016**, 3, 6.
- [20] L. Meli, I. Hussain, M. Aurilio, M. Malvezzi, M. K. O'Malley, D. Pratichizzo, *IEEE Robot. Autom. Lett.* **2018**, 3, 2198.
- [21] S. B. Schorr, A. M. Okamura, *IEEE Trans. Haptics* **2017**, 10, 418.
- [22] F. H. Giraud, S. Joshi, J. Paik, *IEEE Trans. Haptics* **2022**, 15, 131.
- [23] S. Kanjanapas, C. M. Nunez, S. R. Williams, A. M. Okamura, M. Luo, *IEEE Robot. Autom. Lett.* **2019**, 4, 1365.
- [24] E. H. Lee, S. H. Kim, K. S. Yun, *Actuators* **2021**, 10, 60.
- [25] M. T. Thai, T. T. Hoang, P. T. Phan, N. H. Lovell, T. N. Do, *IEEE Access* **2020**, 8, 157878.
- [26] D. K. Y. Chen, I. A. Anderson, C. G. Walker, T. F. Besier, *IEEE Trans. Haptics* **2016**, 9, 62.
- [27] E. Battaglia, J. P. Clark, M. Bianchi, M. G. Catalano, A. Bicchi, M. K. O'Malley, *IEEE Trans. Haptics* **2019**, 12, 508.
- [28] E. Leroy, R. Hinche, H. Shea, *Adv. Mater.* **2020**, 32, 2002564.
- [29] H. Bai, S. Li, R. F. Shepherd, *Adv. Funct. Mater.* **2021**, 31, 2009364.
- [30] M. N. Montandon, W. R. Provancher, presented at 2013 IEEE Int. Conf. Consumer Electronics (ICCE), Berlin, September **2013**.
- [31] C. Wang, D. Y. Huang, S. Hsu, C. E. Hou, Y. L. Chiu, R. C. Chang, J. Y. Lo, B. Y. Chen, presented at 32nd Annual ACM Symp. User Interface Software and Technology, New Orleans, October **2019**.
- [32] A. Ion, E. J. Wang, P. Baudisch, in 33rd Annual Conf. Human Factors in Computing Systems, Seoul, April **2015**.
- [33] N. A. Caswell, R. T. Yardley, M. N. Montandon, W. R. Provancher, presented at 2012 IEEE Haptics Symposium (HAPTICS), Vancouver, March **2012**.

- [1] L. Seminara, P. Gastaldo, S. J. Watt, K. F. Valyear, F. Zuher, F. Mastrogiovanni, *Front. Neurorobot.* **2019**, 13, 53.
- [2] M. N. Nemah, C. Y. Low, O. H. Aldulaymi, P. Ong, A. E. Ismail, A. A. Qasim, *Int. J. Integr. Eng.* **2019**, 11, 299.
- [3] S. Lim, D. Son, J. Kim, Y. B. Lee, J. K. Song, S. Choi, D. J. Lee, J. H. Kim, M. Lee, T. Hyeon, D.-H. Kim, *Adv. Funct. Mater.* **2015**, 25, 375.

- [34] K. Bark, J. Wheeler, G. Lee, J. Savall, M. Cutkosky, presented at World Haptics 2009 – Third Joint EuroHaptics Conf. and Symp. Haptic Interfaces for Virtual Environment and Teleoperator Systems, Washington, March **2009**.
- [35] D. Li, J. Zhou, K. Yao, S. Liu, J. He, J. Su, Q. Qu, Y. Gao, Z. Song, C. Yiu, C. Sha, Z. Sun, B. Zhang, J. Li, L. Huang, C. Xu, T. H. Wong, X. Huang, J. Li, R. Ye, L. Wei, Z. Zhang, X. Guo, Y. Dai, Z. Xie, X. Yu, *Sci. Adv.* **2022**, 8, eade2450.
- [36] F. Pece, J. J. Zarate, V. Vechev, N. Besse, O. Gudozhnik, H. Shea, O. Hilliges, presented at 30th Annual ACM Symp. User Interface Software and Technology, Québec, October **2017**.
- [37] C. Zhang, D. R. Sahoo, J. Pearson, S. Robinson, M. D. Holton, P. Hopkins, M. Jones, presented at 22nd Int. Conf. Human-Computer Interaction with Mobile Devices and Services, Oldenburg, October **2020**.
- [38] Y. H. Jung, J. Y. Yoo, A. Vázquez-Guardado, J. H. Kim, J. T. Kim, H. Luan, M. Park, J. Lim, H. S. Shin, C. J. Su, R. Schloen, J. Trueb, R. Avila, J. K. Chang, D. S. Yang, Y. Park, H. Ryu, H. J. Yoon, G. Lee, H. Jeong, J. U. Kim, A. Akhtar, J. Cornman, T. Kim, Y. Huang, J. A. Rogers, *Nat. Electron.* **2022**, 5, 374.
- [39] H. Culbertson, J. M. Walker, M. Raitor, A. M. Okamura, presented at 2017 CHI Conf. Human Factors in Computing Systems, Denver Colorado, USA, May **2017**.
- [40] V. Arumugam, M. D. Naresh, R. Sanjeevi, *J. Biosci.* **1994**, 19, 307.
- [41] D. H. Kim, N. Lu, R. Ma, Y. S. Kim, R. H. Kim, S. Wang, J. Wu, S. M. Won, H. Tao, A. Islam, K. J. Yu, T. Kim, R. Chowdhury, M. Ying, L. Xu, M. Li, H. J. Chung, H. Keum, M. McCormick, P. Liu, Y. W. Zhang, F. G. Omenetto, Y. Huang, T. Coleman, J. A. Rogers, *Science* **2011**, 333, 838.
- [42] B. V. Johnson, S. Chowdhury, D. J. Cappelleri, *IEEE ASME Trans. Mechatron.* **2020**, 25, 526.
- [43] G. Cui, P. Zhang, X. Liu, L. Xie, W. Huang, P. Pan, J. Qu, Q. Fan, *IEEE Trans. Ind. Electron.* **2023**, 70, 10302.
- [44] Q. Xu, Q. Hu, H. Wang, Z.-H. Mao, M. Sun, *IEEE Trans. Magn.* **2021**, 57, 1.
- [45] S. Zhang, Z. Xia, Z. Liu, Q. Wang, Y. Yue, J. Huang, B. Su, *Chem. Eng. J.* **2023**, 463, 142388.
- [46] F. P. Beer, E. R. Johnston, D. F. Mazurek, in *Vector Mechanics for Engineers. Statics and Dynamics*, 11th ed., McGraw-Hill Education, New York, NY **2016**.
- [47] Y. Huang, Y. Cao, H. Qin, *Adv. Eng. Mater.* **2022**, 24, 2200091.
- [48] Y. Han, J. Dong, *Adv. Mater. Technol.* **2018**, 3, 1700268.
- [49] A. R. Moritz, F. C. Henriques, *Am. J. Pathol.* **1947**, 23, 695.
- [50] Y. Zhou, X. Zhao, J. Xu, Y. Fang, G. Chen, Y. Song, S. Li, J. Chen, *Nat. Mater.* **2021**, 20, 1670.
- [51] X. Zhang, Q. Wang, R. Zou, B. Song, C. Yan, Y. Shi, B. Su, *Eng.* **2022**, 15, 196.
- [52] Y. Yan, Z. Hu, Z. Yang, W. Yuan, C. Song, J. Pan, Y. Shen, *Sci. Robot.* **2021**, 6, eabc8801.
- [53] H. Hu, C. Zhang, C. Pan, H. Dai, H. Sun, Y. Pan, X. Lai, C. Lyu, D. Tang, J. Fu, P. Zhao, *ACS Nano* **2022**, 16, 19271.
- [54] Y. G. Kim, J. H. Song, S. Hong, S. H. Ahn, *Npj Flex. Electron.* **2022**, 6, 52.
- [55] R. Xu, A. Zverev, A. Hung, C. Shen, L. Irie, G. Ding, M. Whitmeyer, L. Ren, B. Griffin, J. Melcher, L. Zheng, X. Zang, M. Sanghadasa, L. Lin, *Microsyst. Nanoeng.* **2018**, 4, 36.
- [56] S. Huang, Y. Liu, Y. Zhao, Z. Ren, C. F. Guo, *Adv. Funct. Mater.* **2019**, 29, 1805924.
- [57] S. Chen, Y. Chen, J. Yang, T. Han, S. Yao, *Npj Flex. Electron.* **2023**, 7, 1.
- [58] C. Hatzfeld, T. A. Kern, in *Engineering Haptic Devices: A Beginner's Guide*, Springer London Limited, London, UK **2014**.